Hydrology and
Earth System
Sciences

Open Access

Supplement of

Identifying recharge under subtle ephemeral features in a flat-lying semi-arid region using a combined geophysical approach

Brady A. Flinchum et al.

Correspondence to: Brady A. Flinchum (brady.flinchum@csiro.au)

Travel-time Tomography Processing

To ensure that we collected the first arrival the data in the field we used a 10 ms buffer prior to the sledgehammer trigger (t₀). The data were collected with 5 m geophone spacing and 5 m shot spacing. The high shot spacing density was selected because, although not shown here, the data were set up for a reflection survey (not discussed in this manuscript) which requires more shots to build common midpoint fold. The profile was running parallel to a well-traveled road connecting Adelaide to Port Wakefield. The highway is approximately 100 m south west of the line. This highway caused unpredictable low-frequency noise on various shots throughout the day (Figure S1).

To reduce the effect of traffic noise we stacked each shot eight times. We also removed a noisy trace at 95 m. First arrivals were picked manually on the stacked shot files (Figures S1). Prior to picking each shot was trace normalized. We attempted to pick as many first-arrivals without the use of a band-pass filter to prevent any shifts caused by the filter at early times. After the arrivals were picked on the raw shot gathers we applied a band-pass filter between 10-120 Hz, which significantly reduced the low frequency traffic noise and allowed us to pick far-offset arrivals (Figure S1). Despite the traffic noise, we were able to confidently pick 2014 travel-times (87% of the data) (Figure S2a).

The travel-time picks were high-quality. The quality of the pick is based on the difference between reciprocal travel times. A reciprocal travel-time occurs when a shot at station x and a receiver at station y is picked, and then later in the data set the shot occurs at station y and the receiver at station x. Theoretically, the difference between these travel-times should be zero, or when plotted they should lie along a 1:1 line (Figure S2c). In our case, because of the high density shot spacing, almost every pick has a reciprocal travel-time and all the reciprocal picks fell within 5 ms of each other (Figure S2a).

We use the reciprocal values to drive the error weight matrix in the PyGIMLi inversion (Rücker et al., 2017). Thus, an error be assigned to every pick. In most cases we used the reciprocal error plus 1.2 ms (ref – why?). In locations where we did not have a reciprocal travel-time we applied a linear function as a function of offset (distance from source). In this case error (in seconds) was defined by Eq. S1 (ref).

$$error = \frac{0.004}{235} offset + 0.0012$$

(Eq. S1)

where offset is simply the distance from the source to the receiver, and the spread length was 235 m. We use Eq. S1 and the calculated reciprocal values to ensure that each pick has an assigned error (Figure 2b). It also provides a way to determine if the data are over fit or under fit. These errors are read into the inversion and used to weight the travel-times during the inversion as well as calculate the χ_2 fit:

$$\chi^2 = \frac{1}{N} \sum_i \frac{(t_{obs} - t_{model})^2}{\sigma_i^2}$$

(Eq. S2)

Where t_{obs} is the observed travel time, t_{model} is the modeled travel time, σ is the picking error, and N is the total number of picks.

With the travel-time picks and associated errors collected we can invert the model. The mesh was selected so that there were at least three nodes between each geophone and the maximum triangle size was no more than 2 m. Based on the slopes of the first arrivals we determined the average velocity was around 2000 m/s. Thus, we used a gradient starting model with 400 m/s at the surface and 2000 m/s at 40 m depth. The depth of the model was selected to not limit the ray paths. This took some experimentation, but the final mesh extends a few meters below the lowest ray path. Smoothing parameters were manually selected through trial and error to achieve a feasible geologic model

and still achieve a good model fit. Specific settings in the the PyGIMLi refraction inversion we set Lambda equal to 200 and the z-weight to 0.5 and the maximum iterations to 5.

Throughout the manuscript we interpret small changes in velocity. Although it is difficult to say exactly how accurate these velocities are, we did attempt to quantify velocity uncertainty. To quantify uncertainty, we took the 2014 travel time picks and randomly removed 30% (604 data points). We used this decimated data set to run an inversion. We would then remove another random 30% of the original data set and invert. This process was repeated 50 times. Each velocity model was saved. At the end all 50 models were averaged together. The average model was run through the forward model to get the travel-times and the error fits. This averaged model is the one shown in the manuscript (Figure 2a). This means that at each model parameter we have a standard deviation, indicating how much it changed (Figure S3c). The standard deviations highlight areas of the highest uncertainty. The values never varied more than 200 m/s (Figure s3c). We are thus confident in the P-wave velocity profile. The final model also outputs the ray coverage. This is the total number of rays that cross through a single model parameter (Figure S3b). This is how we defined the masked region in the main velocity profile (Figure 2). The final model had a χ_2 of 0.82 and a RMS value of 1.73 ms. Both indicate that the modeled travel-times reasonably fit the observed travel times (Figure s3a).

Surface wave Processing

To construct the 2D S-wave velocity profile shown in the manuscript (Figure 3) we used an open source code written in Matlab called Surface Wave Inversion and Profiling (SWIP) (Pasquet and Bodet, 2017). In this section we provide our specific geometry and figures showing the high-quality nature of data to provide a sense of confidence in the final S-wave velocity profile (Figure 3). SWIP uses spatial windowing and frequency stacking to extract local dispersion images representative of 1D slices of the investigated medium, thus detecting more lateral heterogeneity while increasing the signal-to-noise. In this case we extracted dispersion images across 8 traces (Figure S4a). The assumption is that the velocity structure under these 8 traces is horizontally layered and then assigned to the midpoint of the traces. To avoid near-source effects we ensured that there was at least 25 m (5 traces) between the source and the closest geophone. We allowed the source to be up to 115 m away (24 traces) from the first geophone. The code sorts valid pairs of shots and traces through all of the seismic data, then computes dispersion images for each valid shot gathers, and finally stacks all dispersion images corresponding to a single midpoint. On average we stacked ~40 dispersion images per midpoint which generated high quality and easily identifiable dispersion curves (Figure S4b and S4d). Even though we used 14 Hz geophones we had clear energy down to at least 10 Hz (Figure S4b and S4d). The lower frequencies could have been generated from the traffic on the near-by highway.

Based on the shot and geophone geometry we extracted and picked dispersion curves for 41 midpoints every 5 m beginning at 17.5 and ending at 217.5. To show that the low velocity zone between 60-80 m was a clear signal we show two dispersion curves, one from 62.5 m and the other from 162.5 m (Figure S4). During picking it was clear that there were two modes visible (Figure S4). We picked both the fundamental and first higher order mode (Figure S4). It has been shown that higher-order modes can stabilize the inversion and provide additional depth penetration (Xia et al., 2003).To visualize the dispersion picks, they are converted to wavelength using the phase velocity and frequency ($\lambda = v/f$). The picks can be plotted in space for each midpoint (Figure S4e and S4f). The dispersion curve picks for both the fundamental and higher order first mode show a clear pattern and consistency from midpoint to midpoint (Figure S4e and S4f). It should be noted here that the low velocity zone between 60 and 80 m is clear in both modes of the data, and thus should be reflected in the final S-wave velocity profile (Figure S4e and S4f).

The inversion of the surface wave data consists in independent (not laterally constrained from midpoint to midpoint) 1D inversions. The dispersion curve picked at each midpoint are used to in a Monte Carlo inversion scheme. The inversion does three runs of 15000 models each. For each midpoint, the best fitting 1000 S-wave velocity models that replicate the dispersion curves are kept (Figure S5). Thus, for each midpoint we have a suite of models that all converge around a narrow range of a 1D velocity profile (Figure S5a and S5c). The final 1D velocity model is selected by averaging the velocity of top 1000 models. This 1D profile is then used to calculate the theoretical dispersion curves. The modeled dispersion curves fit within our error bars in most cases (Figure S5b and

S5d). The difference between our picks and modeled dispersion curve can then be used to calculate a misfit (Figure S5g). A misfit value below 0.5 is considered adequate. Furthermore, we can visually look at the difference between our picked dispersion curves and modeled dispersion curves (Figure S5e and S5f) to see that the model is representative of the data. The model fits provide confidence in the final 2D velocity model in the manuscript (Figure 3).

Modeling Electrical Conductivity with Archie's Law

The electrical conductivity of the formation (the one that we measure) can be modelled using Archie's Law (Archie, 1941; Robinson et al., 2012).

$$R_{form} = \phi^{-m} S^{-n} R_{fluid},$$
(Eq. S3)

In Eq. S3 φ is porosity, S is saturation, R_{form} is the formation resistivity, R_{fluid} is the fluid resistivity, and conductivity is the inverse of resistivity. The variable m is the cementation coefficient, which accounts for effects of permeability and tortuosity. This value varies between 1.2 and 4.4 (Lesmes and Friedman, 2005; Robinson et al., 2012). The variable n is an empirically defined coefficient but is commonly set at a value of 2 (Knight, 1991; Day-Lewis, 2005; Robinson et al., 2012). Using Archie's equation (Eq. 2) we can explore how the conductivity of the formation will respond as a function of fluid saturation and the conductivity of the fluid. It is often assumed that as the water saturation increases, the fluid conductivity will also increase. We used Archie's law to show that it is possible to observe a drop in electrical conductivity if the pores are being saturated with a more resistive fluid or if a less conductive fluid replaces the higher conductive fluid originally in place.

Using the fully saturated volumetric water content below the water table from the downhole NMR data provides an estimated porosity of 0.25 m3/m3 (Figure 5d). Assuming a soil density of 1.5 provides a porosity estimate of 0.23 m3/m3 from the soil samples collected, which is consistent with the NMR results (Figure 5a). Using equation 2, we calculated the electrical conductivity assuming a fixed porosity of 0.25 m3/m3, setting m to 1.3, setting n to 2, and varying the fluid conductivity from 500 to 4000 mS.m-1 and a saturation from 0 to 1 m3/m3 (Figure 7a).

There are three end-member cases that can be observed from the calculation of the formation conductivity (Figure S7a). The first is filling the pores with water that has the same electrical conductivity as the groundwater (Figure S7a). The result is that the formation conductivity rises exponentially (Figure S7b) and this is consistent with the common interpretation that increasing the saturation also increases the electrical conductivity. The second case is filing the pores with saltier water; that is the fluid filling the pore-space has an increasingly higher electrical conductivity. In this case the formation conductivity also rises exponentially, but at an even faster rate than just filling the pores with water (Figure S7b). The last end member case is filling the pores with fresher water. That is as the saturation increases the fluid conductivity decreases. In this case, it is possible to get a small drop in electrical conductivities (Figure S7b). Furthermore, from this relationship it can be observed that at the same saturation level, the formation conductivity will reduce if the fluid in the pore space is replaced with a more resistive fluid (Figure S7a). This basic forward modelling
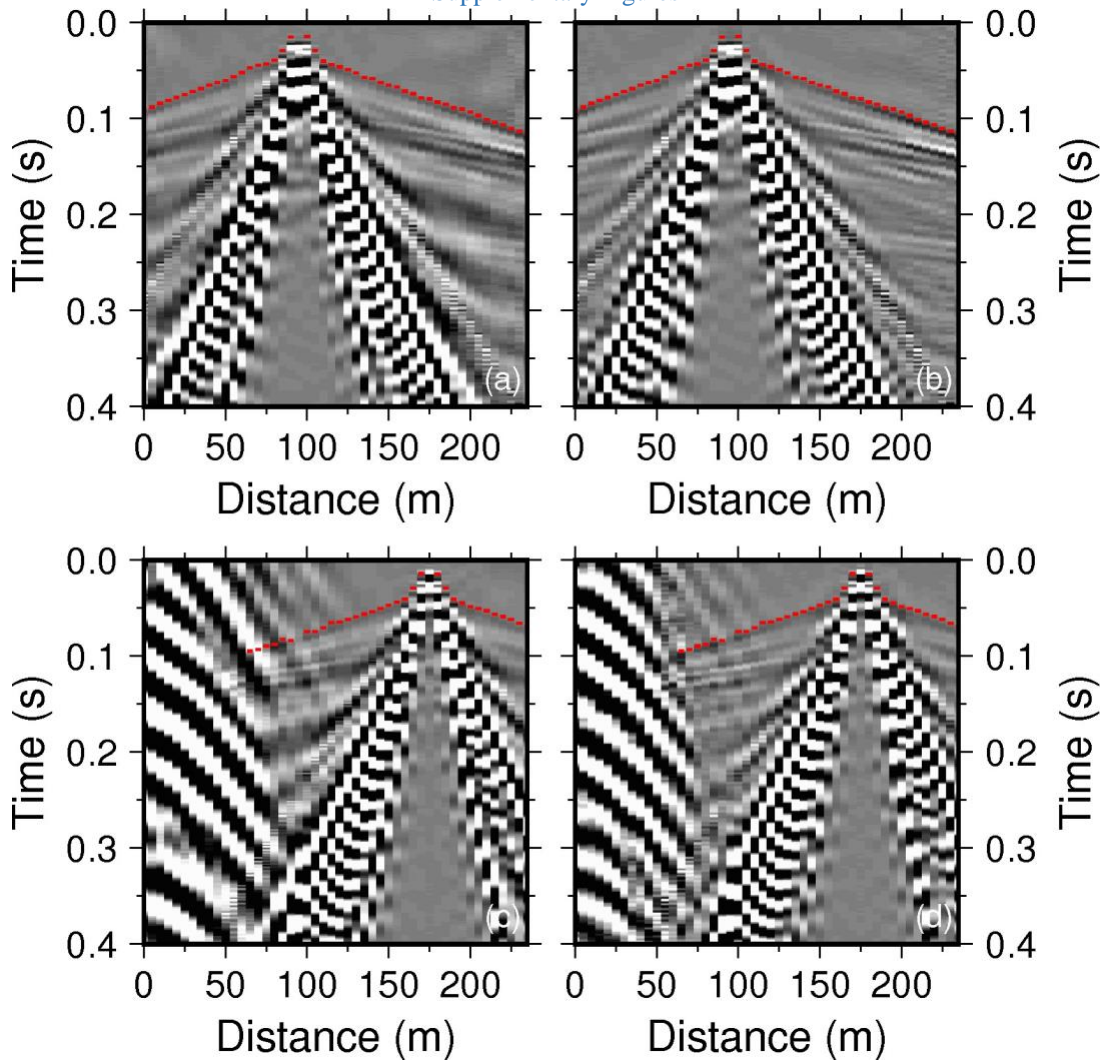
Figure S1
Examples of shot gathers from two shots. The red dashes indicate the first-arrival picks. The top row is a shot from 95 m and illustrates a shot with very little traffic noise. The bottom row shows a shot from 175 m and illustrates a shot with significant traffic noise. (a) Stacked shot gather at 95 m with no band-pass filter. (b) Stacked sho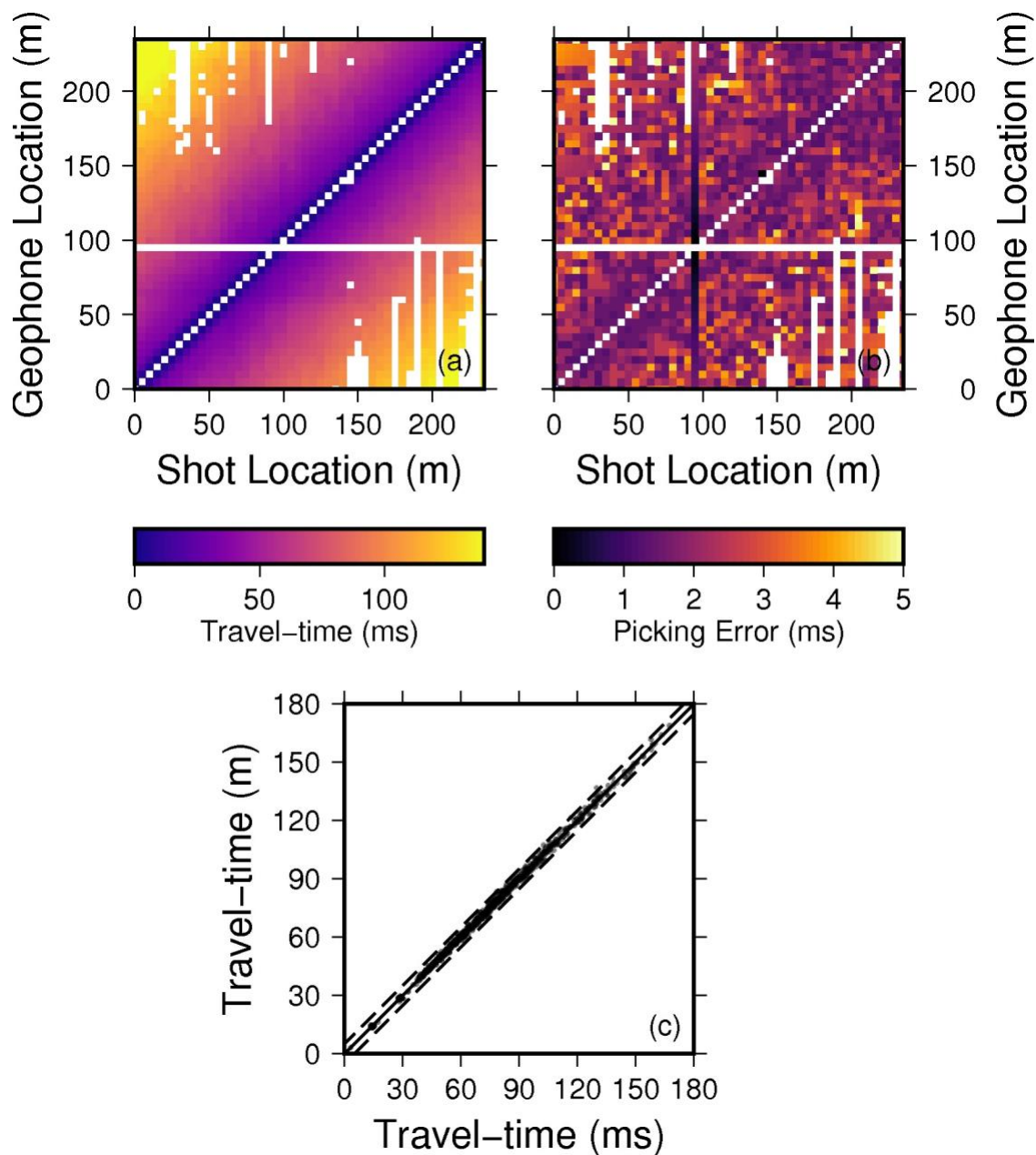t gather at 95 m with the 10-120 Hz bandpass filter applied. (c) Stacked shot gather at 175 m with no band-pass filter. (d) Stacked shot gather at 175 m with the 10-120 Hz bandpass filter applied.

Figure S2
Figures showing the travel-time picks and corresponding errors that drive the inversion. (a) All 2014 travel time picks plotted as a function of shot and geophone location colored by travel-time. The blank horizontal line is the bad geophone at 95 m. The lack of picks at far offsets was caused because of traffic noise. (b) The errors associated with the picks shown in panel a. Any pick without a reciprocal travel-time was assigned using equation S1. (c) Plot of reciprocal travel-times. The x-axis shows the travel time from a shot at x to a receiver at y. The y-axis shows the reciprocal travel-time, that is a shot at y and a receiver at x.
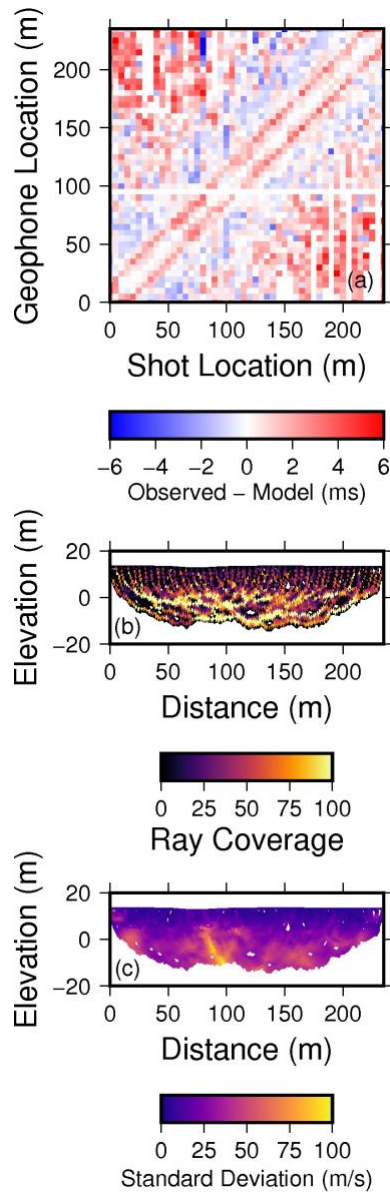
Figure S3
This figure highlights the final model fits to the observed travel-time data. (a) The difference in observed and modeled travel-time for the final model (Figure 2 in main manuscript). The data are plotted spatially according to the shot and geophone location. (b) The total ray coverage for each model parameter in the model. Parameters with no rays are masked out. The colors represent the total number of rays that pass through that model parameter. (c) The corresponding standard deviation calculated from 50 inversions each removing 30% of the travel-time data. Overall the model is very consistent.
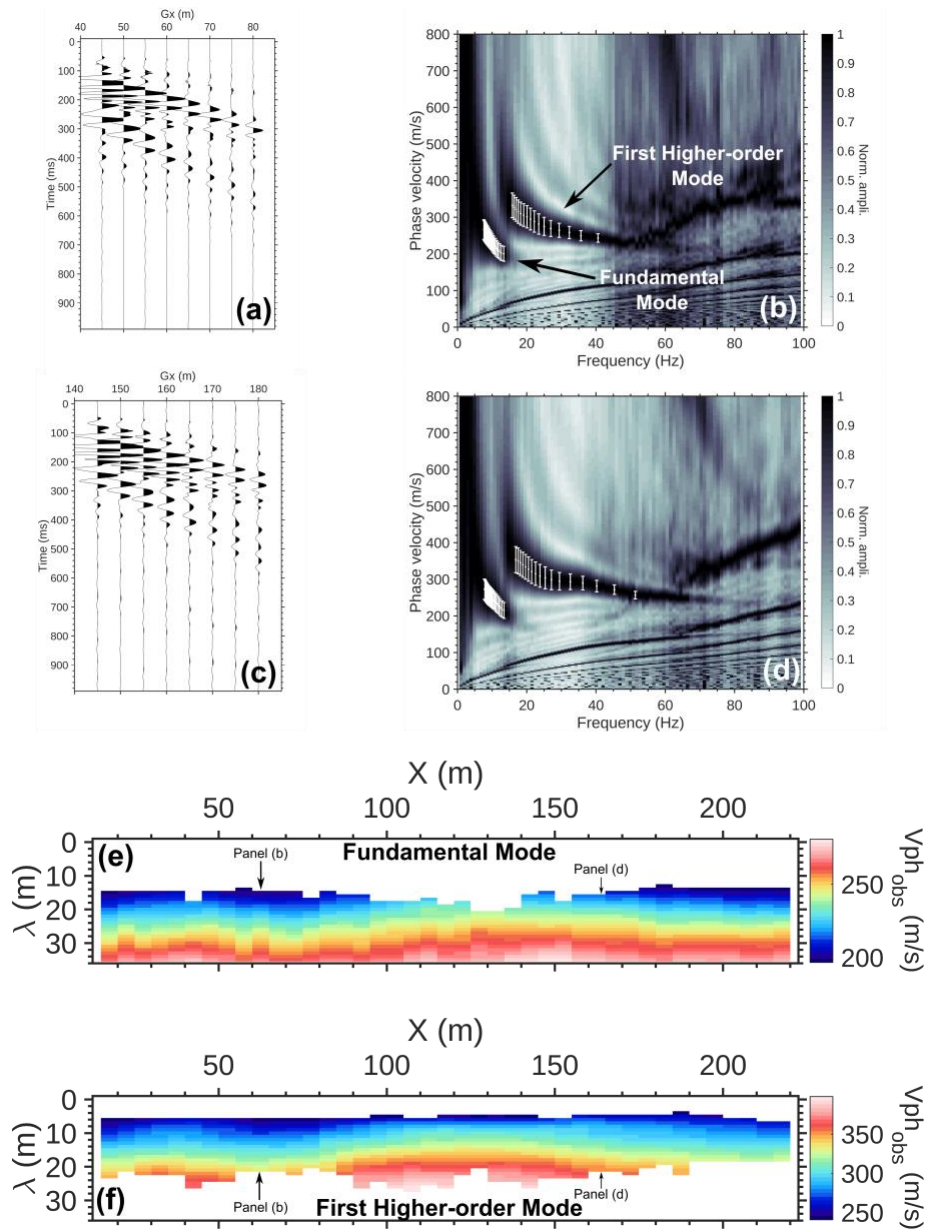
Figure S4.
This figure highlights the high-quality dispersion curves used to create the 2-D S-wave velocity profile in the manuscript (Figure 3). (a) The stacked 8 trace window that has a midpoint of 62.5 m. (b) Dispersion curves for the midpoint at 62.5 m with our picks and errors. The fundamental and first higher-order mode are marked. (c) The stacked 8 trace window that has a midpoint of 162.5 m. (d) Dispersion curves for the midpoint at 162.5 m with our picks and errors. The fundamental and first higher order mode are picked. (e) The fundamental mode picks resampled in 1 m increments and converted to wavelength using the phase velocity and frequency ($\lambda=v/f$). Both panel a and d have been highlighted along this profile. Note the spatial patterns in velocity and continuity from midpoint to midpoint. (f) Same as panel e but for the first-higher order model. Note the low velocity zone between 60-80 m.
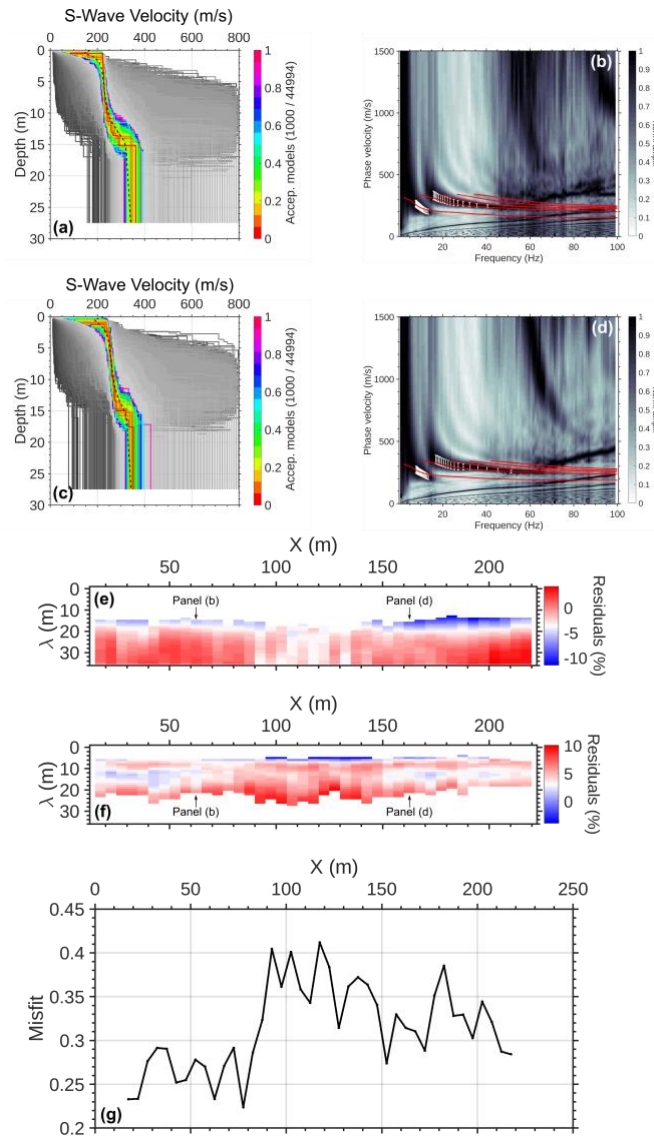
Figure S5.
This figure highlights demonstrates the inversion results for individual midpoints. The final 2D velocity model was generated by averaging the top 1000 models for each midpoint inversion. (a) 1-D S-wave velocity profile showing all 45,000 models that were tried during the MC process for the midpoint at 62.5 m. The best fitting 1000 models are highlighted by color. The average model is shown by a black dotted line. (b) The original dispersion curve and picks (from Figure S4) with the calculated modes from the averaged model plotted in red overlaid for the midpoint at 62.5 m. (c) Same as panel a but for the midpoint at 162.5 m. (d) same as panel b but for the midpoint at 162.5 m. (e) The difference between the observed picks (Figure S4e) and the modeled dispersion curve for the fundamental model. (f) The difference between the observed picks (Figure S4e) and the molded dispersion curve for the first higher-order model. (g) The sum of the differences for both modes plotted spatially for each individual inversion.
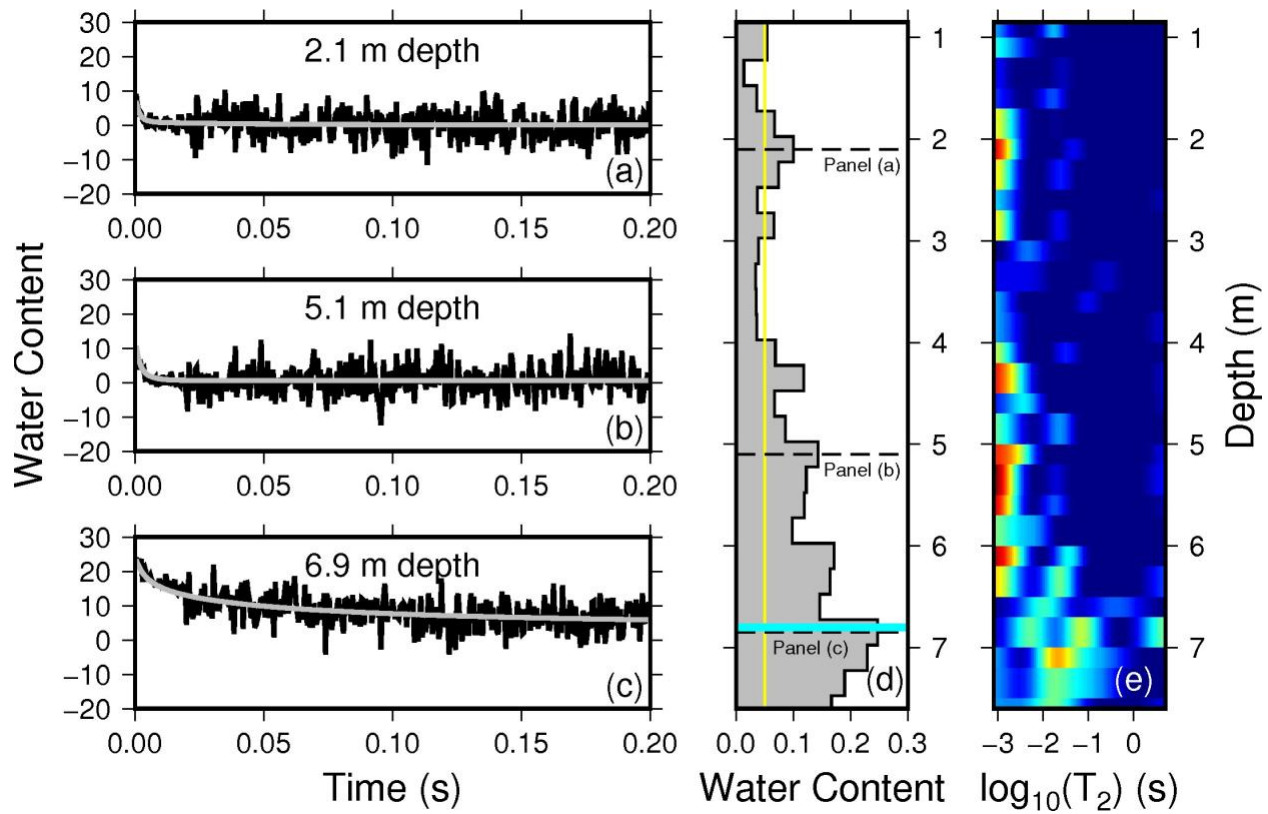
Figure S6
Results from the downhole NMR sounding at the Geoprobe location (Figure 1). Panels a-c show the measured decays in black and the multi-exponential model fits in gray. (a) 2.1 m depth. (b) 5.1 m depth. (c) 6.9 m depth. (d) The inverted water content profile. The thin vertical yellow line shows the average noise level (0.05 m3/m3). Water content values less than this are questionable. The horizontal dashed lines show the locations of panels a-c. The thick horizontal cyan line represents the hand measured water level (6.8 m). (e) The T2 distributions that produced the water content curves in panel d. The maximum water contents are the area under the distribution.
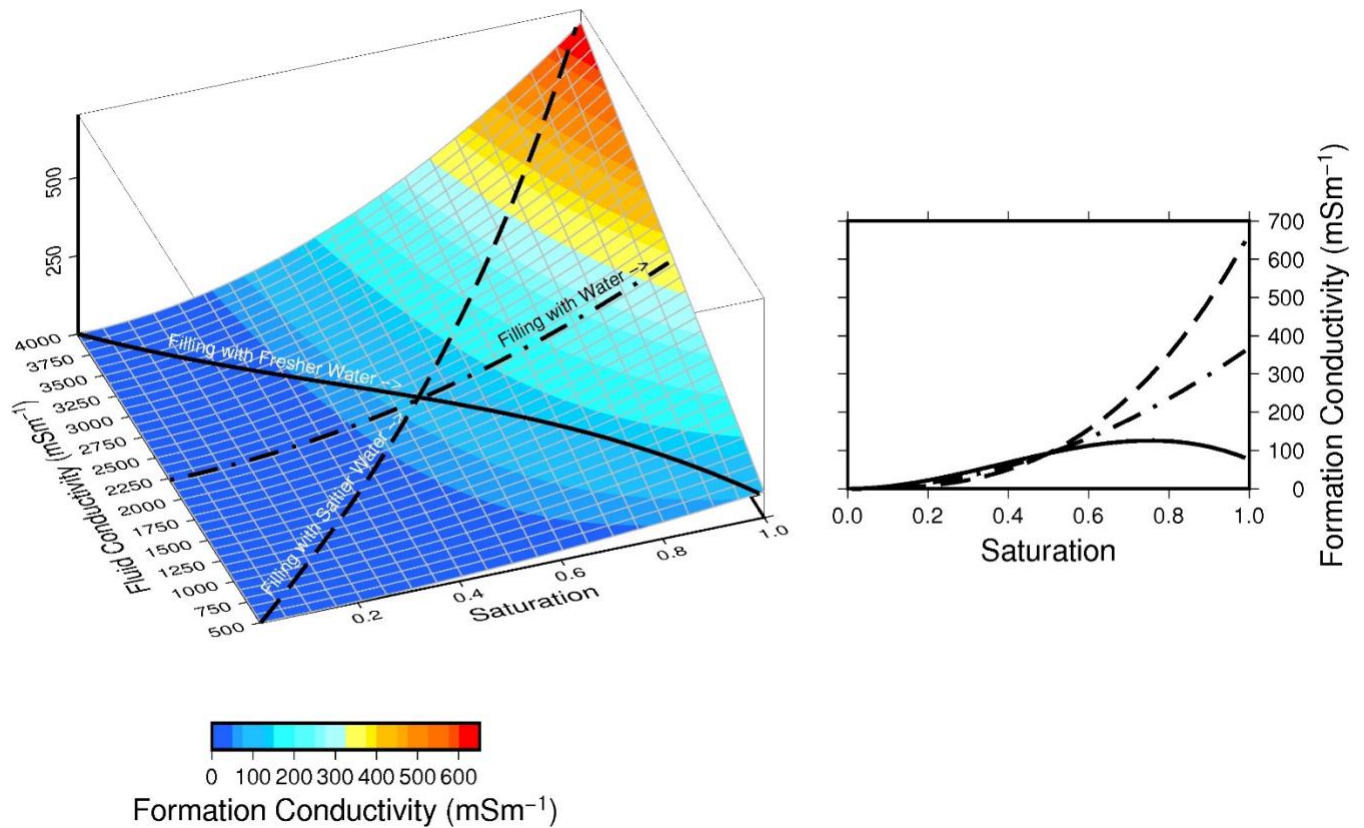
Figure S7.

(a) The relationship between saturation, fluid conductivity, and formation conductivity calculated from Eq. 2, assuming a constant porosity of 0.25, m=1.3, and n =2. The solid black line represents a case where the pore space is being filled with water that gets less conductive (i.e. fresher). The dashed line is a case where water is being replaced with water that gets more conductive (i.e. more saline). The dotted/dashed line is the case of filling the pores with water of the same conductivity. (b) The formation conductivity as a function of saturation for the three end-member cases shown in panel a.

Archie, G.E. 1941. The Electrical Resistivity Log as an Aid in Determining Some Reservoir Characteristics. Trans. Am. Inst. Min. Metall. Eng. 146: 54–61.

Day-Lewis, F.D. 2005. Applying petrophysical models to radar travel time and electrical resistivity tomograms: Resolution-dependent limitations. J. Geophys. Res. 110(B8): B08206. doi: 10.1029/2004JB003569.

Knight, R. 1991. Hysteresis in the electrical resistivity of partially saturated sandstones. GEOPHYSICS 56(12): 2139–2147. doi: 10.1190/1.1443028.

Lesmes, D.P., and S.P. Friedman. 2005. Relationships between the Electrical and Hydrogeological Properties of Rocks and Soils. In: Rubin, Y. and Hubbard, S.S., editors, Hydrogeophysics. Springer Netherlands, Dordrecht. p. 87–128

Pasquet, S., and L. Bodet. 2017. SWIP: An integrated workflow for surface-wave dispersion inversion and profiling. Geophysics 82(6): WB47–WB61. doi: 10.1190/geo2016-0625.1.

Robinson, J.L., L.D. Slater, and K.V.R. Schäfer. 2012. Evidence for spatial variability in hydraulic redistribution within an oak–pine forest from resistivity imaging. J. Hydrol. 430–431: 69–79. doi: 10.1016/j.jhydrol.2012.02.002.

Rücker, C., T. Günther, and F.M. Wagner. 2017. pyGIMLi: An open-source library for modelling and inversion in geophysics. Comput. Geosci. 109: 106–123. doi: 10.1016/j.cageo.2017.07.011.

Xia, J., R.D. Miller, C.B. Park, and G. Tian. 2003. Inversion of high frequency surface waves with fundamental and higher modes. J. Appl. Geophys. 52(1): 45–57. doi: 10.1016/S0926-9851(02)00239-2.